# ChemComm

# A reconstruction strategy to synthesize mesoporous SAPO molecular sieve single crystals with high MTO catalytic activity†

Chan Wang,‡[a] Miao Yang,‡[a] Mingrun Li,[b] Shutao Xu,[a] Yue Yang,[a] Peng Tian*[a] and Zhongmin Liu*[a]

**Mesoporous SAPO-34 single crystals with tunable porosity and Si content have been fast synthesized within 4 hours by a reconstruction strategy, which show excellent hydrothermal stability and MTO catalytic activity. This new strategy is further proven to be applicable to prepare other mesoporous SAPO molecular sieve single crystals.**

Zeolites and silicoaluminophosphate (SAPO) molecular sieve with a unique microporous structure and acidity are important solid acid catalysts which have been widely used in many industrial processes, such as oil refining and petrochemistry.[1,2] However, the sole presence of micropores often imposes diffusion limitation which leads to low utilization of the catalyst active centers and fast coke deposition, resulting in a short catalytic lifetime. Integrating mesopores into microporous structures is believed to be an effective solution for this problem.[3–5] Many related synthetic strategies, including bottom-up directing construction by soft or hard templates and top-down post-synthetic acid/base treatments, have been developed. Unfortunately, the process of manufacture of mesoporous structures damages the integrity of microporous structures in most cases, which makes it difficult to maintain the essential microporosity and acidity comparable to those of conventional microporous molecular sieve.[6] Worse still, the hydrothermal stability decreases much due to the amorphous structure of the mesoporous channel wall. It is highly desirable to fabricate crystallized mesoporous walls so that hierarchical porosity, intrinsic acidity and hydrothermal stability can be integrated in one material.[5] For this, several new types of multifunctional soft templates including quaternary ammonium-type organosilane[7] and gemini-type polyquaternary ammonium surfactants[8–10] have been developed,

by which mesoporous zeolites ZSM-5[7,8] and A,[7] and aluminophosphate molecular sieves AlPO-5, -11 and -31[10] have been synthesized successfully. Moreover, a nonsurfactant cationic polymer polydiallyldimethylammonium chloride has also been developed as an effective two-in-one template to synthesize mesoporous beta single crystals with excellent hydrothermal stability and catalytic activity.[11] Nevertheless, it is still a challenge to create highly active mesoporous SAPO molecular sieve single crystals by a soft-template method. The presence of a mesoporogen brings severe interference for the crystallization of SAPO molecular sieves. The crystallization will get slow and impurities are easy to form. It is thus difficult to achieve high crystallinity and desired hierarchical porosity simultaneously for the aimed product. As a result, the crystallinity and composition optimization have to be sacrificed in most cases for the synthesized hierarchical SAPO molecular sieves, and their catalytic performance remains less improved even though the diffusion limitation has been relieved.[12,13]

In this work, we have developed a new reconstruction strategy to synthesize mesoporous SAPO molecular sieve single crystals. The crystallization of mesoporous SAPO-34 can be completed within 4 hours, and the phase region is quite wide. Notably, the obtained mesoporous SAPO-34 is proved to be a single crystal phase possessing excellent hydrothermal stability, which has alterable composition and textural properties. The MTO catalytic stability is thus significantly improved. In addition, mesoporous SAPO-11 and DNL-6 molecular sieves have also been fast synthesized by this method.

The present synthesis procedure involves the use of a mesoporogen and quite an amount of milled SAPO-34 precursor. The introduction of the SAPO-34 precursor could greatly accelerate the crystallization of the microporous structure and make it match well with the fast formation of mesopores. Moreover, it counteracts the side effect caused by the mesoporogen and widens the phase region as much as possible. For details, [3-(trimethoxysilyl)propyl]octadecyldimethylammonium chloride (TPOAC), Al(i-C$_3$H$_7$O)$_3$, H$_3$PO$_4$, TEOS, diethylamine (DEA) and water were firstly mixed in sequence. After that, a certain amount

[a] *National Engineering Laboratory for Methanol to Olefins, Dalian National Laboratory for Clean Energy, Dalian Institute of Chemical Physics, Chinese Academy of Sciences, Dalian 116023, China. E-mail: tianpeng@dicp.ac.cn, liuzm@dicp.ac.cn*

[b] *State Key Laboratory of Catalysis, Dalian Institute of Chemical Physics, Chinese Academy of Sciences, Dalian 116023, China*

† Electronic supplementary information (ESI) available. See DOI: 10.1039/c6cc01834c
‡ These authors contributed equally to this work.

of milled SAPO-34 precursor was added. The mixture was sealed in an autoclave and heated at 200 °C for 4 hours. Finally, the product was collected by centrifugation, washed and dried in air. A series of mesoporous SAPO-34s with various Si content and textural porosities have been synthesized by changing the reaction compositions (see ESI†). The samples were evaluated by the MTO catalytic reaction, and the optimized one was picked out to do more characterizations, which was designated as SP34-MS. For comparison, another SAPO-34 with comparable composition was also synthesized by introducing the milled SAPO-34 precursor, but without the use of a mesoporogen. The sample was named SP34-P (for more details see the ESI†).

Both SP34-MS and SP34-P have well-resolved XRD patterns indexed to the highly crystalline CHA structure (Fig. S1, ESI†). However, they have quite different morphology, as shown in Fig. 1a, b and Fig. S2 (ESI†). The crystals of SP34-P are intergrown by multiple micrometer-sized SAPO-34 crystals which form the secondary particles of around 3 μm, while SP34-MS presents uniform dice-like particles in the size range of 300–500 nm. It is very interesting to note that the surface of the SP34-MS crystal is quite rough. It consists of a large number of 20–50 nm nanocrystals with abundant holes. The crystals were further crushed and characterized by SEM. It is found that the crystal interior is the same as the external surface (Fig. 1c). $N_2$ adsorption isotherms and pore size distribution curves are depicted in Fig. 1d and e, respectively. SP34-P shows a typical I-type isotherm for microporous materials, while SP34-MS gives I plus IV type isotherms suggesting the coexistence of micropores and mesopores. A significant enhanced uptake and a

**Table 1** Textural properties of the samples

| Sample | $S_{BET}$[b] $(m^2\ g^{-1})$ | $S_{mic}$[c] $(m^2\ g^{-1})$ | $S_{ext}$[c] $(m^2\ g^{-1})$ | $V_{mic}$[c] $(cm^3\ g^{-1})$ | $V_{meso}$[d] $(cm^3\ g^{-1})$ |
|---|---|---|---|---|---|
| SP34-MS | 567 | 455 | 112 | 0.21 | 0.17 |
| SP34-MS-HT[a] | 450 | 400 | 50 | 0.20 | 0.15 |
| SP34-P | 602 | 593 | 9 | 0.28 | 0.02 |

[a] SP34-MS after 100% steam treatment at 800 °C for 17 h. [b] Total surface area is determined using the BET equation. [c] Micropore surface area, volume and external surface area are determined by the t-plot method. [d] Mesopore volume is determined from the adsorption isotherm by the BJH method.

pronounced hysteresis loop at $0.4 < P/P_0 < 0.9$ are observed for SP34-MS owing to the capillary condensation in the mesopores. The mesopore size distribution of SP34-MS is centered at 4.7 nm. The textural properties of the two samples are exhibited in Table 1. SP34-MS exhibits an apparently larger external surface area of 112 $m^2\ g^{-1}$ and a higher mesopore volume of 0.17 $cm^3\ g^{-1}$ suggesting the existence of the mesoporous structure.

Variable-temperature laser-hyperpolarized (HP) $^{129}Xe$ NMR is a very sensitive technique to check the geometry and connectivity of the porous structures.[14,15] So, it was herein used to explore the porosities of the samples. Mesoporous silica (named $SiO_2$) with mesopore size distribution at 4.5 nm (Fig. S3, ESI†), and a mechanical mixture of SAPO-34 and mesoporous silica (named mixture) were taken as reference samples. The mixture has very similar textural properties to that of SP34-MS (Fig. S3 and Table S1, ESI†). HP $^{129}Xe$ NMR spectra of the four samples at various temperatures are shown in Fig. S4 (ESI†). Fig. 1f illustrates their HP $^{129}Xe$ NMR spectra at 173 K. For mesoporous $SiO_2$, the signal at 109 ppm is attributed to the adsorbed Xe in the mesopores. Because SP34-P is a pure microporous material, its two $^{129}Xe$ signals at 200 and 149 ppm should arise from the adsorbed Xe in the microporous CHA structure. The appearance of more than one signal is due to the sensitivity for the different number of Xe atoms absorbed in the micropores.[16] Accordingly, the two downfield signals at 190 and 148 ppm of SP34-MS are due to the absorbed Xe in the CHA microporous structure, while the upfield line at 115 ppm is ascribed to adsorbed Xe in the mesopores. The mixture has a comparable HP $^{129}Xe$ NMR spectrum with that of SP34-MS. However, the chemical shift distance ($\Delta\delta$) between micropore and mesopore signals is 33 ppm for SP34-MS, which is less than that of the mechanically mixed one (40 ppm). The results suggest that the Xe exchange between the micropores and mesopores in SP34-MS is faster than in the mechanically mixed counterpart. 2D-exchange spectroscopy (EXSY) NMR spectra were further measured to confirm this. As illustrated in Fig. S5 (ESI†), the cross-signals of 148 and 115 ppm peaks can be easily detected for SP34-MS in 2 ms mixing time, while they are absent for the mechanically mixed one. It is thus believed that SP34-MS has good channel connectivity between micropores and mesopores.

Transmission electron microscopy (TEM) was taken to further characterize SP34-MS. Many irregular pores are visible under low magnification (Fig. 2a and b). The thin zone of the crystal edge was selected to take the high-resolution TEM
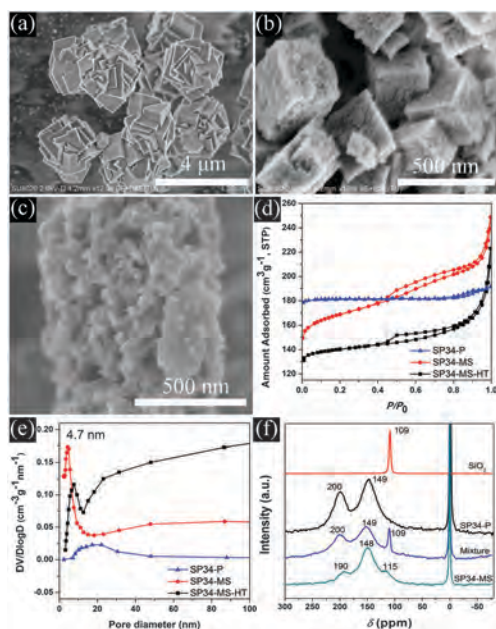


**Fig. 1** SEM images of calcined (a) SP34-P, (b) SP34-MS and (c) broken crystals of SP34-MS. (d) $N_2$ sorption isotherms and (e) pore size distribution calculated from the adsorption branch of calcined SP34-P, SP34-MS and SP34-MS-HT. (f) Laser-hyperpolarized $^{129}Xe$ NMR spectra of Xe adsorbed in mesoporous silica ($SiO_2$), SP34-P, mechanical mixture and SP34-MS at 173 K.
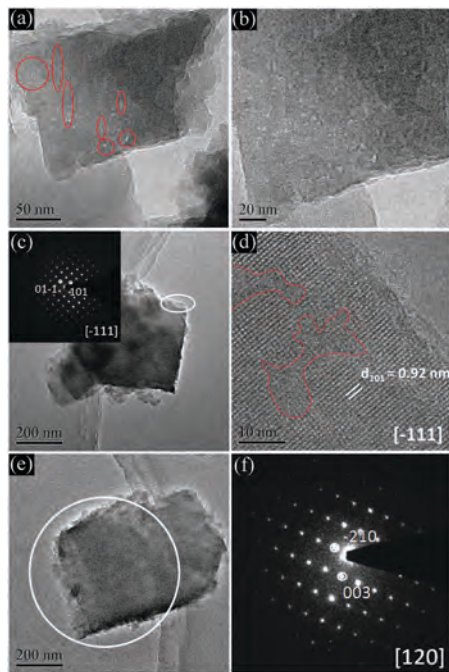
Fig. 2 (a and b) TEM images of SP34-MS under low magnification. (c) TEM image and SAED pattern (inset) of SP34-MS taken along the [−111] zone axis. (d) HRTEM image of SP34-MS corresponding to the circle region in (c). (e) TEM image of individual SP34-MS crystals. (f) SAED pattern taken with the selected circle region of (e) and along the [120] zone axis.
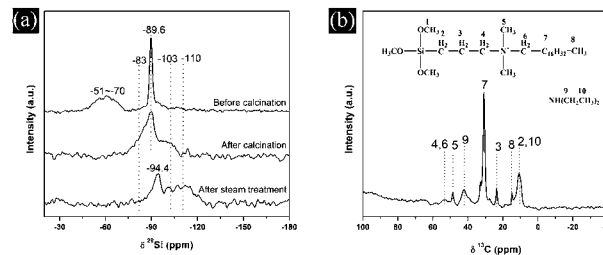


Fig. 3 (a) $^{29}$Si CP NMR spectrum of as-synthesized SP34-MS, $^{29}$Si MAS NMR spectra for calcined and steam treated SP34-MS. (b) $^{13}$C MAS NMR spectrum of as-synthesized SP34-MS.

(HRTEM) and selected area electron diffraction (SAED). There are clear crystal lattice fringes with consistent orientation in the HRTEM image (Fig. 2d). The spacing of the atomic layers is 0.92 nm corresponding to the (101) plane. 4–10 nm mesopores can be identified in the HRTEM image which break the continuous microporous structure. The results agree with the characterization of $N_2$ adsorption and HP $^{129}$Xe NMR measurements. Interestingly, the SAED pattern (inset of Fig. 2c) gives highly discrete diffraction spots suggesting a single crystal feature. More individual crystals were picked out to take the SAED in large selected area and along various directions. All the images (Fig. 2e, f and Fig. S6, ESI†) give individual diffraction patterns confirming the single crystal nature of the product.

Hydrothermal stability is a fatal weakness for mesoporous materials because of their disordered channel wall structure. When the material becomes a mesoporous single crystal, the channel wall is an actually ordered microporous framework structure, whose hydrothermal stability is expected to be considerably improved. In the present study, the hydrothermal stability of SP34-MS was assessed by exposing it to 100% steam at 800 °C for 17 h. The sample after treatment, denoted as SP34-MS-HT, has a nearly unchanged XRD pattern (Fig. S1, ESI†), morphology (Fig. S7, ESI†) and $N_2$ adsorption isotherms (Fig. 1d). The crystallinity of SP34-MS-HT remains 80% though the external surface area decreases some (see Table 1). It exhibits a better hydrothermal stability than other hierarchical SAPO-34 molecular sieve.[17]

Solid-state NMR measurements were used to characterize the chemical environments of SP34-MS. The $^{29}$Si CP NMR spectrum

of as-synthesized SP34-MS (Fig. 3a) gives a clear resonance signal at −89.6 ppm due to $Si(OAl)_4$ species.[18] A broad signal at −51 to −70 ppm is detected and ascribed to the $T_n$ groups ($T_n = RSi(OAl)_n(OH)_{3−n}$, R = organic groups, $n$ = 2 and 3).[19,20] This suggests that the organo-siloxane groups coming from mesoporogen TPOAC are condensed into the SAPO framework. The existence of the organic part is further confirmed by the $^{13}$C NMR MAS spectrum (Fig. 3b). After calcination, the $T_n$ signal in the $^{29}$Si spectrum disappears due to the removal of TPOAC. Besides, a shoulder peak at around −83 ppm and a broad peak near −103 ppm arise which correspond to the newly formed $Si(OAl)_n(OH)_{4−n}$ ($n$ = 1, 2) and $Si(OSi)_n(OAl)_{4−n}$ ($n$ = 1–3) species, respectively.[18,20] The Si environment further changes after the hydrothermal treatment (800 °C for 17 h). The main $^{29}$Si signal shifts to −94.4 ppm, together with the appearance of a broad signal at around −110 ppm due to the formation of Si islands. High-temperature steam treatment leads to the atomic migration, dehydroxylation and the change of bond lengths and angles. These variations are responsible for the change in the Si environments which agree with the results of conventional SAPO-34.[21,22]

The catalytic properties of SP34-P, SP34-MS and SP34-MS-HT were evaluated in the MTO reaction. The results are presented in Table 2 and Fig. S8 (ESI†). SP34-MS exhibits excellent catalytic performance. The methanol conversion over 99% can be kept for 480 min, which is more than twice as long as that of microporous SP34-P. Their selectivity for ethylene plus propylene is comparable (82.1% *vs.* 81.9%). After hydrothermal treatment, the catalytic lifetime of SP34-MS-HT is prolonged to 530 min, and the selectivity of ethylene and propylene increases to 83.8%. $NH_3$-TPD was measured to check the acidity of these samples. The results (Fig. S9, ESI†) indicate that SP34-MS has a comparable acid strength with that of SP34-P, but its acidic concentration is much lower than that of SP34-P. After hydrothermal treatment, the acid concentration of SP34-MS-HT decreases further due to the formation of large Si islands, while its acid strength is still well kept. It is thus believed that the decreased acid concentration and enhanced diffusion efficiency associated with SP34-MS are responsible for the enhancement of MTO catalytic performance. And the single crystal nature of the sample helps the hydrothermally treated SP34-MS-HT in holding the excellent catalytic activity. As a comparison, our previously synthesized hierarchical SAPO-34[23] was also hydrothermally treated and tested in the MTO reaction. The catalytic lifetime

**Table 2** Lifetime[a], product selectivity[b] in the MTO reaction over SAPO-34s before and after steam treatment at 800 °C for 17 h

| Sample | Lifetime (min) | $C_2^=$ (%) | $C_3^=$ (%) | $C_2^= + C_3^=$ (%) |
|---|---|---|---|---|
| SP34-MS | 480 | 49 | 33.1 | 82.1 |
| SP34-MS-HT | 530 | 58.1 | 25.7 | 83.8 |
| SP34-P | 225 | 48.3 | 33.6 | 81.9 |
| SAPO-34 nanosheet assembly[c] | 308 | 49.7 | 31.4 | 81.1 |
| SAPO-34 nanosheet assembly-HT[d] | 191 | 51.8 | 31.2 | 83.0 |

[a] Experimental conditions: WHSV = 3 h$^{-1}$, $T$ = 450 °C, catalyst weight = 300 mg. The catalyst lifetime is defined as the reaction duration with >99% methanol conversion. [b] The highest selectivity of ethene and propene under >99% methanol conversion. [c] Sample 7 in ref. 23. [d] SAPO-34 nanosheet assembly after treatment with 100% steam at 800 °C for 17 h.

of this sample drastically reduced after the hydrothermal treatment (see Table 2), which clearly demonstrates the advantages of mesoporous SAPO-34 single crystals synthesized by the reconstruction method.

In order to understand the reconstruction method, a series of mesoporous SAPO-34s synthesized using different SiO$_2$/Al$_2$O$_3$ and starting amounts of milled SAPO-34 precursor were prepared and the synthetic results are illustrated in Table S2 and Fig. S10 (ESI†). Notably, the crystallization region is quite wide, and the molar ratio of SiO$_2$/Al$_2$O$_3$ in reactant gel can be changed from 0.2 to 0.6. The product Si content rises as the increasing amount of milled SAPO-34 precursor for the samples synthesized with constant silica and aluminum sources. It is deduced that the increased Si content is contributed by the milled SAPO-34 precursor which was integrated into the products. Besides the contribution to the composition, the precursor also helps to modify the textural properties. The BET surface area and micropore volume increase, and the external surface area and mesopore volume decrease with the increase of the precursor. This is likely due to the greatly improved growth rate of microporous structures by the presence of the precursor, which suppresses the generation of mesoporosity. So the double introduction of a suitable amount of milled SAPO-34 precursor together with the quaternary ammonium-type organosilane would be the key to success which makes the crystallization of microporous and mesoporous structures match well.

The reconstruction method is further developed to prepare other SAPO molecular sieve single crystals, and mesoporous SAPO-11 and DNL-6 have also been successfully synthesized. More synthesis and characterization details are given in ESI† including Table S3 and Fig. S11, S12.

In summary, we have demonstrated a reconstruction approach for the fast synthesis of mesoporous SAPO molecular sieves. For the first time, an unusual mesoporous SAPO-34 single crystal phase has been achieved by the combined use of a milled SAPO-34 precursor and a mesoprogen, which accelerates the growth rate of microporous structures and implants mesopores simultaneously. The sample exhibits good hydrothermal stability and excellent MTO catalytic stability. This new synthetic strategy has been proven to be applicable to the synthesis of other mesoporous SAPO molecular sieve single crystals.

## Notes and references

1 A. Corma, *Chem. Rev.*, 1995, **95**, 559–614.
2 H. van Bekkum, E. M. Flanigen, P. A. Jacobs and J. C. Jansen, *Introduction to zeolite science and practice*, Elsevier, Amsterdam, 2001.
3 J. Perez-Ramirez, C. H. Christensen, K. Egeblad, C. H. Christensen and J. C. Groen, *Chem. Soc. Rev.*, 2008, **37**, 2530–2542.
4 K. Na, M. Choi and R. Ryoo, *Microporous Mesoporous Mater.*, 2013, **166**, 3–19.
5 K. Moller and T. Bein, *Chem. Soc. Rev.*, 2013, **42**, 3689–3707.
6 S. Mitchell, M. Milina, R. Verel, M. Hernandez-Rodriguez, A. B. Pinar, L. B. McCusker and J. Perez-Ramirez, *Chem. – Eur. J.*, 2015, **21**, 14156–14164.
7 M. Choi, H. S. Cho, R. Srivastava, C. Venkatesan, D. H. Choi and R. Ryoo, *Nat. Mater.*, 2006, **5**, 718–723.
8 M. Choi, K. Na, J. Kim, Y. Sakamoto, O. Terasaki and R. Ryoo, *Nature*, 2009, **461**, 246–249.
9 K. Na, C. Jo, J. Kim, K. Cho, J. Jung, Y. Seo, R. J. Messinger, B. F. Chmelka and R. Ryoo, *Science*, 2011, **333**, 328–332.
10 Y. Seo, S. Lee, C. Jo and R. Ryoo, *J. Am. Chem. Soc.*, 2013, **135**, 8806–8809.
11 J. Zhu, Y. H. Zhu, L. K. Zhu, M. Rigutto, A. van der Made, C. G. Yang, S. X. Pan, L. Wang, L. F. Zhu, Y. Y. Jin, Q. Sun, Q. M. Wu, X. J. Meng, D. L. Zhang, Y. Han, J. X. Li, Y. Y. Chu, A. M. Zheng, S. L. Qiu, X. M. Zheng and F. S. Xiao, *J. Am. Chem. Soc.*, 2014, **136**, 2503–2510.
12 Y. L. Liu, L. Z. Wang and J. L. Zhang, *Mater. Lett.*, 2011, **65**, 2209–2212.
13 L. L. Wu and E. J. M. Hensen, *Catal. Today*, 2014, **235**, 160–168.
14 I. L. Mourdrakovski, V. V. Terskikh, C. I. Ratcliffe, J. A. Ripmeester, L. Q. Wang, Y. Shin and G. J. Exarhos, *J. Phys. Chem. B*, 2002, **106**, 5938–5946.
15 Y. Liu, W. P. Zhang, Z. C. Liu, S. T. Xu, Y. D. Wang, Z. K. Xie, X. W. Han and X. H. Bao, *J. Phys. Chem. C*, 2008, **112**, 15375–15381.
16 C. J. Jameson, A. K. Jameson, R. Gerald and A. C. Dedios, *J. Chem. Phys.*, 1992, **96**, 1676–1689.
17 J. Zhu, Y. Cui, Y. Wang and F. Wei, *Chem. Commun.*, 2009, 3282–3284.
18 W. L. Shen, X. Li, Y. X. Wei, P. Tian, F. Deng, X. W. Han and X. H. Bao, *Microporous Mesoporous Mater.*, 2012, **158**, 19–25.
19 T. M. Suzuki, T. Nakamura, E. Sudo, Y. Akimoto and K. Yano, *J. Catal.*, 2008, **258**, 265–272.
20 Z. T. Xue, J. H. Ma, W. M. Hao, X. Bai, Y. H. Kang, J. H. Liu and R. F. Li, *J. Mater. Chem.*, 2012, **22**, 2532–2538.
21 M. Briend, R. Vomscheid, M. J. Peltre, P. P. Man and D. Barthomeuf, *J. Phys. Chem.*, 1995, **99**, 8270–8276.
22 Z. M. Liu, X. Y. Huang, C. Q. He, Y. Yang, L. X. Yang and G. Y. Cai, *Chin. J. Catal.*, 1996, **17**, 540–543.
23 C. Wang, M. Yang, P. Tian, S. T. Xu, Y. Yang, D. H. Wang, Y. Y. Yuan and Z. M. Liu, *J. Mater. Chem. A*, 2015, **3**, 5608–5616.